# Supplementary information for: Single-shot Kramers–Kronig complex orbital angular momentum spectrum retrieval

Zhongzheng Lin,[1,*] Jianqi Hu,[2,*,†] Yujie Chen,[1] Camille-Sophie Brès[2] & Siyuan Yu[1,‡]

[1] *State Key Laboratory of Optoelectronic Materials and Technologies, School of Electronics and Information Technology, Sun Yat-sen University, Guangzhou 510275, China.*

[2] *École Polytechnique Fédérale de Lausanne, Photonic Systems Laboratory (PHOSL), STI-IEM, Station 11, Lausanne CH-1015, Switzerland.*

[*] *These authors contributed equally to the work*

[†] *Email: jianqi.hu@epfl.ch*

[‡] *Email: yusy@mail.sysu.edu.cn*

## Supplementary Note 1. Experimental setup

Fig. S1 illustrates the experimental setup used for Kramers-Kronig (KK) complex orbital angular momentum (OAM) spectrum retrieval. A continuous-wave laser at $1550$ nm is collimated, and polarization managed to match the working-axis of the spatial light modulator (SLM). The collimated beam is then split into the reference path and the signal path via a beam splitter. The signal field used in the experiment is prepared in a 4-f system with a SLM at its input plane and an iris at its Fourier plane. Such a configuration allows for the synthesis of arbitrary complex OAM fields[42]. The OAM field under test is co-axially combined with the reference beam via another beam splitter. A neutral density filter is inserted in the reference path to adjust its optical power. At the output of the $4$-f system, the camera captures the interferogram of the signal and the reference beams. The system is aligned on-axis before actual measurements are taken. By scanning the center of the interferogram and calculate the average retrieval accuracy for a few known OAM fields, we determine its center as the position that registers the highest accuracy.

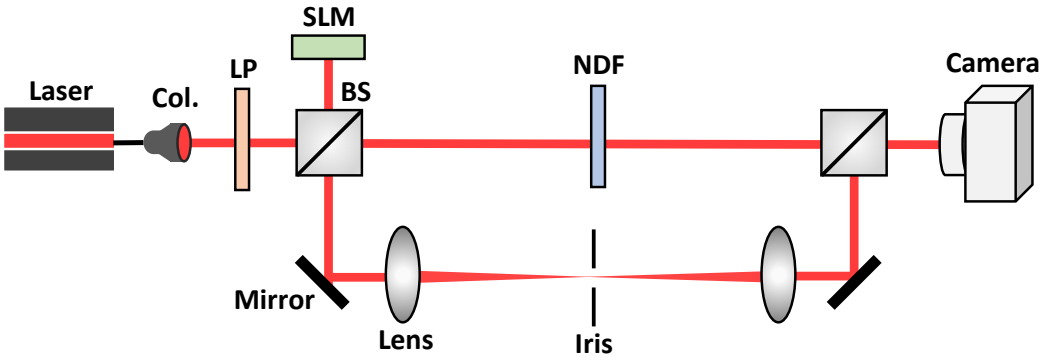


**Fig S1:** Experimental setup for KK complex OAM spectrum retrieval. Col.: collimator; LP: linear polarizer; BS: beam splitter; SLM: spatial light modulator; NDF: neutral density filter.

The OAM mode basis used in this work is the ring-shaped perfect vortex mode, which can be approximately represented as[39]:

$$E(r,\phi) = e^{-\frac{(r-r_0)^2}{w_0^2}} e^{il\phi} \tag{S1}$$

where $r_0$, $w_0$ are the radius and half-width of the ring, respectively. In the experiment, $r_0 = 750\ \mu\text{m}$, $w_0 = 150\ \mu\text{m}$ are chosen for the OAM measurement space with topological charges spanning from 1 to 20. When the dimensionality is enlarged to 30, the beam parameters are readjusted to $r_0 = 1000\ \mu\text{m}$, $w_0 = 200\ \mu\text{m}$ . The reference beam is collimated and can be considered to have a Gaussian profile $E_r(r,\phi) = e^{-r^2/w^2}$ on the plane of the camera, with a beam radius $w = 1100\ \mu\text{m}$.

## Supplementary Note 2. Control of the carrier-to-signal power ratio

In this section, we discuss how we experimentally control the carrier-to-signal power ratio (CSPR) in the OAM spectrum retrieval process. Noticeably, for different complex states, the CSPRs required to satisfy the minimum phase condition are different. In the following, we show that, by using the arbitrary OAM field synthesis method described above[42], the difference between the experimental CSPR and the minimum required CSPR is well maintained automatically for all cases.

The signal field is generated by carving the input Gaussian beam into the target field structure through a computer-generated hologram (CGH). Since the synthesized OAM states possess identical radial distributions, we only consider their distributions in the azimuthal angle:

$$E_s(\phi) = \sqrt{P_0\gamma}a(\phi)e^{i\varphi(\phi)}, \tag{S2}$$

where $P_0$ is the power of the ring-shaped beam with flat phase profile, and $\gamma$ denotes the diffraction efficiency that generates the CGH. $a(\phi)$ and $\varphi(\phi)$ represent the relative amplitude and phase distributions of the target OAM states, respectively. Here the amplitude $a(\phi)$ is normalized such that $\max\{a(\phi)\} = 1$ for $\phi \in [0, 2\pi)$. To meet the minimum phase condition, the reference amplitude needs to be greater than the peak amplitude of the signal field[31]. This sets the minimum CSPR required for the measurement:

$$\mathrm{CSPR_m} = 10\log\frac{\max|E_s(\phi)|^2}{P_s} = 10\log\frac{P_c\gamma}{P_s}, \tag{S3}$$

where $P_s =< |E_s(\phi)|^2 >$ is the power of the signal field average in the azimuthal angle. The difference between the experimental CSPR and the minimum required CSPR writes:

$$\mathrm{CSPR} - \mathrm{CSPR_m} = 10\log\frac{P_c}{P_s} - 10\log\frac{P_0\gamma}{P_s} = 10\log\frac{P_c}{P_0\gamma}. \tag{S4}$$

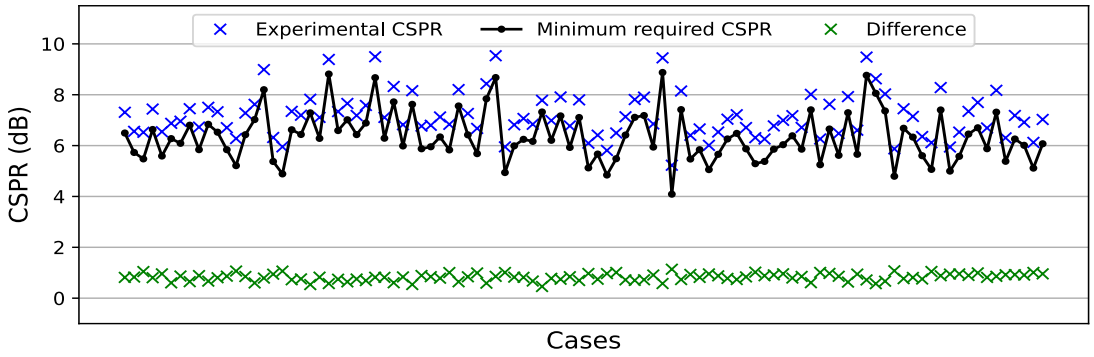


**Fig S2:** Experimentally measured CSPRs, minimum required CSPRs and their differences for 100 random complex OAM states. The experimental CSPRs are slightly higher than the minimum required CSPR values, and their differences are roughly kept the same for different cases.

We can see that the difference here only depends on the diffraction efficiency $\gamma$. By keeping $\gamma$ constant throughout the experiment, we can always ensure the experimental CSPR to be slightly

higher than the minimum required CSPR value. In practice, we usually keep their difference around 1 dB. Fig. S2 shows the CSPR conditions for 100 random OAM fields [one tenth of the fields in Fig. 5(a) in the main text]. The CSPR difference is well maintained for distinct OAM spectra.

In scenarios where the experimental CSPR needs to be changed, instead of varying the attenuation for the reference beam, we can also adjust the diffraction efficiency $\gamma$ of the CGH. In this way, the signal power is varied thereby effectively changing the CSPR. This digital method allows for a more controlled adjustment of the experimental CSPR, which does not affect the alignment of the setup. For instance, when studying the retrieval performance at different CSPR levels (corresponding to Fig. 4 in the main text), the signal power is decreased in steps of $0.5$ dB by varying the diffraction efficiency $\gamma$.

**Supplementary Note 3. Effect of upsampling**

The logarithmic operation taken in the KK retrieval procedure expands the bandwidth of the OAM spectrum[31]. If the number of physical sampling points in the azimuthal angle does not cover the broadened spectrum, digital upsampling is necessary to ensure accurate retrieval. The upsampling is implemented on the normalized interferogram $|E_i(\phi)|^2/|E_r(\phi)|^2$, by means of zero-padding in the Fourier domain[32]. After the Hilbert transformation and necessary computations, the data is downsampled to the original number of samples.

In the following, we show the effect of upsampling in simulation, for retrieving the same complex OAM spectrum as in Fig. 2 of the main text. To demonstrate its full retrieval capability, the complex field with OAM mode indices from 1 to 20 is sampled at the Nyquist frequency (41 azimuthal samples). Fig. S3(a) shows the retrieved OAM spectra without and with upsampling of different factors. It can be seen that, without upsampling, the retrieved field cannot reproduce perfectly the target spectrum. The accuracy of the retrieval (defined as the overlap integral of the retrieved field and the ground truth) remains low in this case ($\sim 0.81$), as quantified in Fig.

S3(b) with $\text{error} = 1 - \text{accuracy}$. However, only $3$-times digital upsampling could significantly boost the accuracy to $0.99$, which is also manifested by the retrieved OAM spectrum. While almost perfect retrieval can be reached by further increasing the upsampling factor to $11$-times. As shown in Fig. S3(b), the error is minimized and the accuracy is converged to unity with a higher upsampling factor. It is worth to mention that, unlike time signals in optical communications, the number of azimuthal samples here is a relatively small value given by the OAM measurement spectral range. As such, the digital upsampling does not add much computational complexity to the retrieval process.

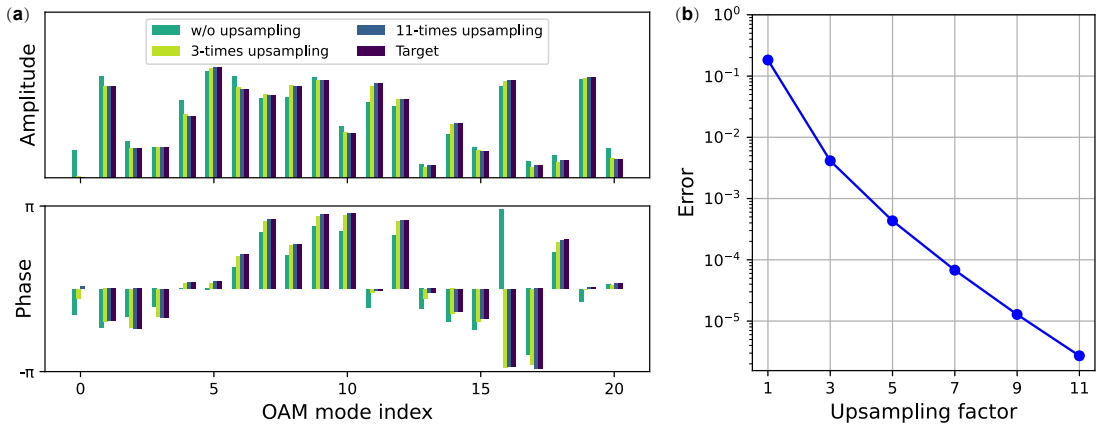


**Fig S3:** Effect of digital upsampling on the KK retrieval performance. (a) The amplitude and phase of the retrieved OAM spectrum without, and with $3$-times and $11$-times digital upsampling. (b) The error of the retrieved complex OAM spectrum versus the upsampling factor. The retrieval accuracy improves with the increase of the digital upsampling.

## Supplementary Note 4. Retrieval workflow and sample code

To more clearly illustrate the workflow of the KK method, a step-by-step flow chart is illustrated as shown in Fig. S4. A sample code for simulating the retrieval of a random OAM spectrum is also provided in https://github.com/GeorgeCravis/OAM-KK.

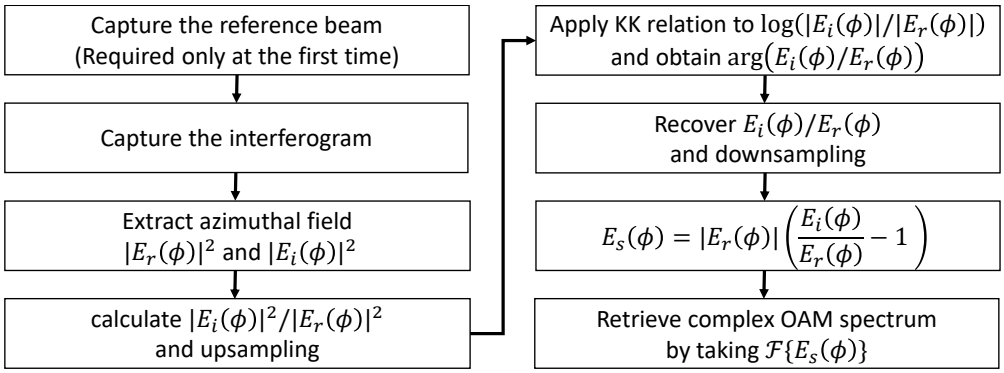


**Fig S4:** Workflow of the KK retrieval method.

## Supplementary Note 5. Details of the Fourier method

In the main text, we compare the performances of the KK and Fourier methods. Here we give the implementation detail of the Fourier method. By taking the Fourier transform of Eq. (2) in the main text, one yields:

$$\begin{aligned}\mathcal{F}\{|E_i(\phi)|^2\} &= \mathcal{F}\{A^2\} + \mathcal{F}\{|E_s(\phi)|^2\} + Ae^{-i\theta_r}\mathcal{F}\{E_s(\phi)\} + Ae^{i\theta_r}\mathcal{F}\{E_s^*(\phi)\} \\ &\approx \mathcal{F}\{A^2\} + Ae^{-i\theta_r}\mathcal{F}\{E_s(\phi)\} + Ae^{i\theta_r}\mathcal{F}\{E_s^*(\phi)\},\end{aligned} \tag{S5}$$

where $\mathcal{F}\{\}$ denotes the Fourier transform. In essence, the Fourier method neglects the SSBI term, as seen in the second row of Eq. (S5). Such an approximation is valid when the reference beam is much stronger than the signal beam (large CSPR), which facilitates the retrieval of the complex field of the signal beam. Note that $\mathcal{F}\{A^2\}$ represents the zero-th order in the OAM spectrum, while $Ae^{-i\theta_r}\mathcal{F}\{E_s(\phi)\}$ and $Ae^{i\theta_r}\mathcal{F}\{E_s^*(\phi)\}$ correspond to the positive and negative sides of the spectrum, respectively, without overlapping each other. As such, the complex amplitude of each OAM component of the signal beam can be obtained, simply by looking at the positive OAM spectral components of $|E_i(\phi)|^2$.

Fig. S5 shows the simulated retrieval performance of the Fourier method under different CSPR values, and is compared to the performance of KK retrieval. Here the signal field under test is the same as in Fig. 3(a) (also Fig. 4) used in the main text. The shaded area represents the possible range of retrieval accuracy when the relative phase between the reference and signal

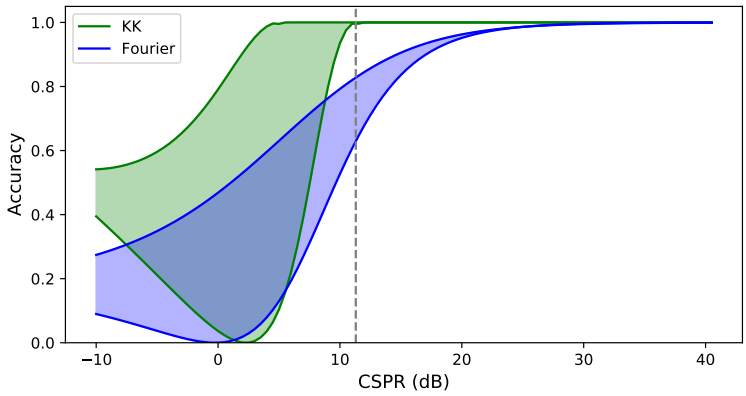


**Fig S5:** Retrieval performances of KK method and Fourier method under different CSPR values. The signal field under test is the same as Fig. 3(a) in the main text. The shaded area represents the possible range of retrieval accuracy when the relative phase between the reference and signal beam is varied. The dashed vertical line indicates the minimum CSPR required for perfect retrieval using KK method.

beam is varied (the same effect is experimentally shown in Fig. 4(c) in the main text for KK retrieval). Unlike being rigorous retrieval as in the KK case, the Fourier method only approximates the ground truth. The accuracy of the Fourier retrieval gradually approaches unity with the increase of the CSPR, as the SSBI gradually becomes less significant compared to other terms. For decent reconstruction, the CSPR required by the Fourier method is around 10 dB higher than what is needed for the KK method (vertical dashed line). At the threshold CSPR value for KK method, the accuracy using the Fourier method falls between 60% to 80%. In Fig. 5 of the main text, we work slightly above the CSPR threshold.

## Supplementary Note 6. Comparison with off-axis holography

Fig. S6 shows the conceptual diagrams of various schemes related to our OAM KK diagnosis, including the conventional off-axis holography (a), KK off-axis holography (b), the counterpart of conventional off-axis holography in OAM (c-d), and our method (e-f) being the counterpart of KK off-axis holography in OAM. In conventional off-axis holography, the SSBI and singnal-reference interference parts need to be well separated in the wavevector space to ensure the precise

retrieval of the signal full-field. Fig. S6(a) shows the critical condition where the spatial frequency contents of SSBI and the signal shifted by the reference are tangent, setting the minimum bound for the off-axis angle. Such a measurement is at the cost of requiring finer sampling resolution to accommodate larger $k$-space information. KK off-axis holography uses the KK relation, instead of the Fourier transform, to recover the signal full-field[32]. In this case, the KK relation can still rigorously retrieve the signal at scenarios when the Fourier contents of SSBI and the shifted signal are largely overlapped. Fig. S6(b) shows the critical condition when the SSBI and the two shifted signal parts take the same length in $k_x$-axis. Compared to the conventional off-axis holography, this approach requires less sampling resolution since a smaller off-axis angle can be used.

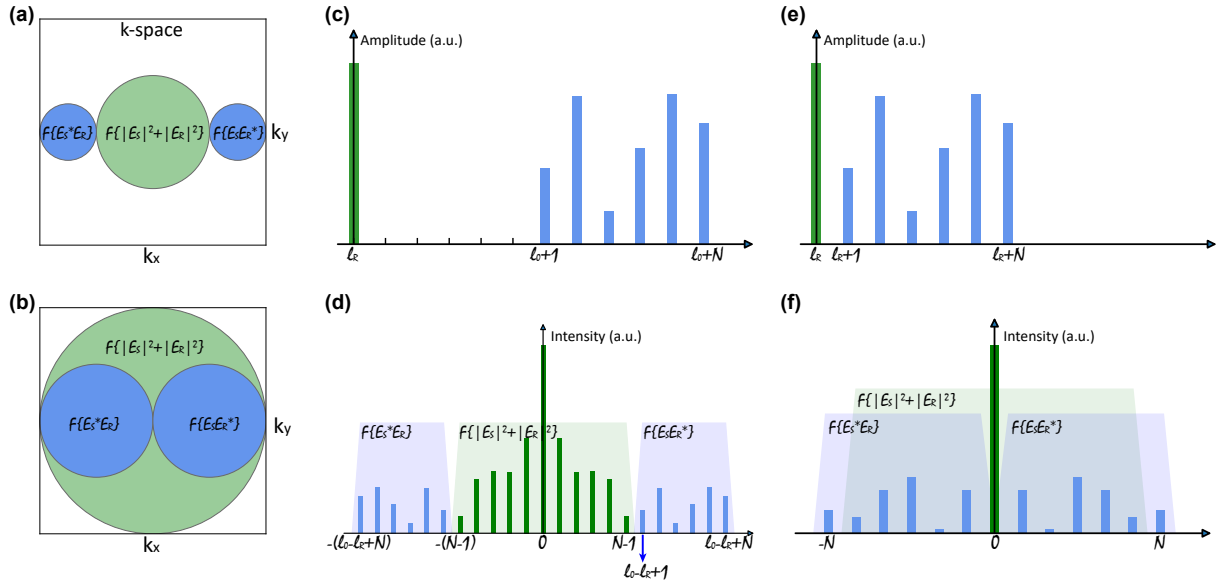


**Fig S6:** Conceptual diagrams of off-axis holography and on-axis OAM analyzers. The wavevector space representations of (a) conventional and (b) KK off-axis holography, which use Fourier and KK relations to reconstruct the signal field, respectively. The OAM space representations of the reference and the signal field (c) with and (e) without a OAM guard band, whose intensity of interferograms are illustrated in (d) and (f), respectively. On-axis OAM analyzer (d) uses Fourier method to retrieve the complex OAM spectrum and is the OAM counterpart of conventional off-axis holography (a), while (f) uses KK retrieval and is the OAM counterpart of KK off-axis holography (b).

In contrast, the approach we take in this work is on-axis interferometry, applied for charac-

terizing OAM fields. The on-axis configuration is not only simpler but also allows for retrieval with optimal sampling at Nyquist frequency. In order to rigorously retrieve both the amplitude and phase information from intensity-only measurement, past demonstrations use phase shifting methods which require multiple shots. Alternatively, single shot retrieval is indeed possible but needs a substantial spacing between the reference mode and the signal OAM field. This is illustrated in Fig. S6(c), when considering the recovery of an arbitrary OAM field spanning over $N$ modes with indices in the range $[l_0+1, l_0+N]$, with a reference OAM mode at index $l_r$. The OAM content after intensity detection is shown in Fig. S6(d). The SSBI occupies the OAM modes in $[-N+1, N-1]$, while the desired interference terms populate the mode space $[\pm(l_0+1-l_r), \pm(l_0+N-l_r)]$. Similar to off-axis holography, rigorous retrieval necessitates the desired interference to be well separated from SSBI, setting the requirement $l_0 + 1 - l_r \geq N$. In other words, there must be at least $(N-1)$ void modes in between the reference and the signal field of OAM bandwidth of $N$. As such, a large OAM mode space is wasted, and requires two-times of Nyquist sampling to account for the guard band. In fact, this scheme is the OAM counterpart of conventional off-axis holography depicted in Fig. S6(a), where the transverse wavevector is replaced by the OAM mode.

To bypass the need of OAM guard band, we study in this work a new OAM full-field retrieval method using KK relation, inspired by the KK retrieval in space[32] and time[28]. Due to its one-dimension nature, the use of KK in OAM actually resembles more of that in time, which has been extensively explored in coherent communications recently. As illustrated in the main text and Fig. S6(e), no OAM guard band is needed between the reference and signal fields. Fig. S6(f) shows the OAM spectrum of the intensity of the interferogram, where the desired interference is largely overlapped with SSBI. Nevertheless, once the CSPR condition and Nyquist sampling are met, the KK retrieval can still rigorously recover the OAM full-field, as in KK off-axis holography and KK receiver in optical communications.

In Fig. S7 we visualize the difference between our OAM KK method with KK off-axis holography. We consider the full-field retrieval of a superimposed perfect vortex beam $E_s(\phi) = 3e^{i5\phi} + 8e^{i15\phi} + 16e^{i30\phi}$ as an example. In the wavevector space, different OAM orders are clearly

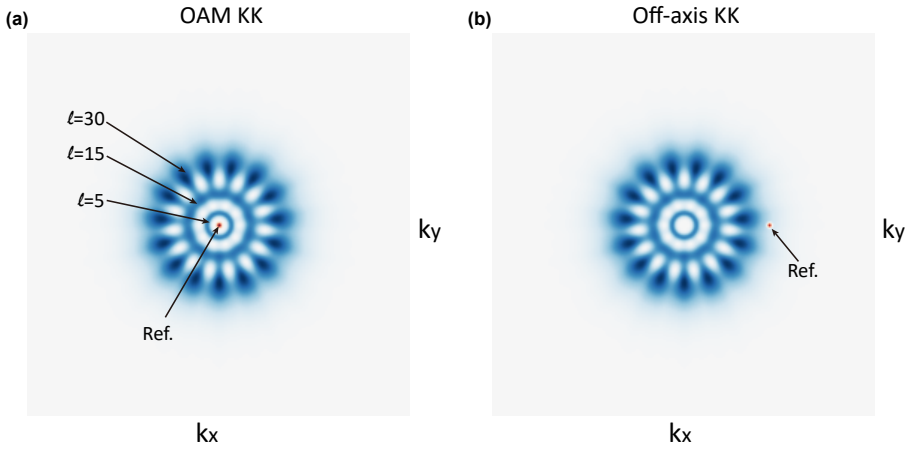


**Fig S7:** Visualization of the OAM KK method and KK off-axis holography in the wavevector space. The Fourier transform of the perfect vortex field $E_s(\phi) = 3e^{i5\phi} + 8e^{i15\phi} + 16e^{i30\phi}$ is shown as an example. (a) With OAM KK method, the reference field can be at the center of the wavevector space if Gaussian beam is used. (b) In KK off-axis holography, the wavevector of the reference field needs to be outside of the signal's spectrum in the wavevector space.

observed and indicated. For our OAM KK method, we use an on-axis Gaussian beam as the reference field, corresponding to a spot in the center of the Fourier space as shown in Fig. S7(a). Evidently, this violates the condition for KK off-axis holography, which requires the wavevector of the reference to be outside of the signal field shown in Fig. S7(b). In fact, the reference OAM mode in our approach can take arbitrary negative topological charge. As such, the reference field may lie completely within the signal field in the wavevector space. Compared to KK off-axis holography, OAM KK approach is favored when characterizing perfect vortex fields of narrow beam widths. This is due to the fact that these fields exhibit Bessel kind of distributions in the radial direction of the Fourier space, thus requiring a high sampling resolution when KK off-axis holography is employed.

In the following, we also quantitatively compare the OAM measurement bandwidths of our OAM KK method and the conventional off-axis holography, in the context of perfect vortex (PV) beams . For OAM KK method, the number of azimuthal samples varies at different radii $r$, which

can be approximated as $2\pi r/\Delta p$ with $\Delta p$ the pixel pitch of the camera. According to the Nyquist sampling theorem, the highest order of the OAM modes that can be retrieved at the radius of $r_0$ is:

$$l_{kk} \approx \frac{\pi r_0}{\Delta p}. \tag{S6}$$

Now we consider the case of conventional off-axis holography that spatially separate the signal from SSBI in the Fourier domain. As shown in Fig. S6(a), the SSBI bandwidth is twice as large as that of the signal beam. To maximally utilize the bandwidth of the camera, the signal beam is diagonally modulated by the reference beam. This yields the maximally allowed bandwidth of the signal as[32]:

$$B_s = \frac{2}{(2+3\sqrt{2})\Delta p}. \tag{S7}$$

The bandwidth of the PV mode can be obtained by its Fourier relationship with the Bessel mode. For the PV mode of order $l$ and radius of $r_0$, its Fourier transform is given by[39]:

$$\widetilde{E}_{PV}(\rho,\theta) \sim J_l(2\pi r_0\rho)e^{il\theta}, \tag{S8}$$

where $(\rho,\theta)$ are the radial distance and angle in polar coordinates of the Fourier plane. $J_l$ denotes the $l^{th}$-order Bessel function of the first kind. The Bessel beam described by Eq. (S8) exhibits concentric ring-shaped intensity distribution with its power mostly confined to the first circle. Since $J_{-l}(2\pi r_0\rho) = (-1)^l J_l(2\pi r_0\rho)$, the $+l$ and $-l$ orders have the same intensity distributions in the Fourier plane. Without loss of generality, we discuss only the positive OAM spectrum part. To approximate the bandwidth of the PV mode, we take the first zero point of the Bessel beam as the radius in the Fourier plane:

$$\rho_l = j_l/2\pi r_0, \tag{S9}$$

where $j_l$ represents the first zero point of the $l^{th}$-order Bessel function of the first kind. For $l > 0$, $j_l$ as well as the bandwidth of the $l^{th}$-order PV mode increase monotonically with $l$. In the range of interest ($1 \leq l \leq 200$ in our case), the first zero of the $J_l$ can be approximately fitted as $j_l \approx l + 5$. In order to be retrieved by the conventional off-axis holography, the bandwidth of the PV mode should be within its maximum measurement bandwidth, i.e. $\rho < B_s/2$. The factor of $1/2$ comes

from the fact that $B_s$ is the diameter while $\rho$ is the radius. As such, the highest OAM order that can be retrieved is derived:

$$l_{oa} \approx \frac{2\pi r_0}{(2+3\sqrt{2})\Delta p} - 5. \tag{S10}$$

As the $+l$ and $-l$ OAM orders have the same intensity distributions, the actual number of modes that can be retrieved range from $-l_{oa}$ to $l_{oa}$. In total around $2l_{oa}$ of OAM modes can be measured by the conventional off-axis holography. When $r_0/\Delta p$ (the radius in pixel unit) is large, the constant term in $l_{oa}$ may be omitted. The ratio between the number of OAM modes that can be retrieved by our KK method and conventional off-axis holography is thus given $l_{kk}/2l_{oa} \approx \frac{2+3\sqrt{2}}{4}$. The OAM KK method outperforms the conventional off-axis holography method by a factor of $l_{kk}/2l_{oa} \approx 1.6$ in terms of the OAM measurement bandwidth.

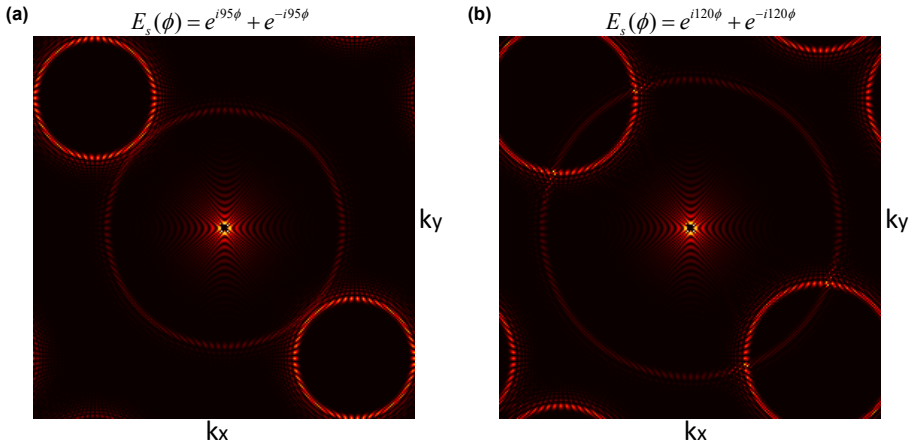


**Fig S8:** The Fourier plane distributions of the interferograms using the conventional off-axis holography. The signal field under test for (a) $E_s(\phi) = e^{-i95\phi} + e^{i95\phi}$; (b) $E_s(\phi) = e^{-i120\phi} + e^{i120\phi}$. The zero frequency component in the center of the image is removed for better image contrast.

We use the following example to clearly show the performance difference between the two methods. When $r/\Delta p = 100$, there are 656 samples in the azimuthal angle, determining the OAM measurement bandwidth as $328$ modes. However, according to Eq. (S10), the measurement range of the conventional off-axis holography ranges from $-95$ to $95$ order, in total 191 modes. When the signal field is $E_s(\phi) = e^{-i95\phi} + e^{i95\phi}$, its Fourier plane distribution using the conventional

off-axis holography is shown Fig. S8(a). It can be clearly seen that the circle of the SSBI is tangential to the circle of the signal, indicating that the current situation is exactly at the limit. The zero frequency component in the center of the image is removed for better image contrast. Further increasing the OAM order of the signal field will result in the failure of the conventional off-axis holographic retrieval. This is visualized in Fig. S8(b) where the signal field under test is $E_s(\phi) = e^{-i120\phi} + e^{i120\phi}$. The signal and SSBI components appear to be mixed and there is also the aliasing problem, thereby they cannot be effectively separated in the Fourier plane.

**Supplementary Note 7. Choice of the radius for azimuthal sampling**

In the experiment, we choose the sampling radius the same as the radius of the PV modes, where the PV modes have the maximum intensity. However, the choice of sampling radius for PV beams is quite flexible as long as the minimum CSPR and Nyquist sampling conditions are met. First, we discuss the CSPR condition when varying the sampling radius. Due to different radial distributions of the Gaussian beam (beam waist radius of $1100\ \mu\mathrm{m}$) and perfect vortex modes (radius of $750\ \mu\mathrm{m}$), the CSPR value changes with the sampling radius. Fig. S9(a) and (b) shows their radial intensity distributions and the corresponding CSPR values, respectively.

At the sampling radius of $750\ \mu\mathrm{m}$ we studied, the intensity of the Gaussian mode is around 1 dB higher than the perfect vortex mode, slightly above the minimum required CSPR. In fact, this is almost the radius with the lowest CSPR, meaning that the minimum phase condition can be easily satisfied at other radii to achieve the ideal retrieval. In our experiments, we still choose the radius of 750 μm to maximize the visibility of the intensity of interferogram, so as to fully utilize the dynamic range of the camera.

Apart from the CSPR condition, the rigorous retrieval also needs to satisfy the Nyquist sampling theorem. Notably, the number of azimuthal samples varies at different radii for 2D images, shown in Fig. S9(c). This will determine the highest OAM order that can be retrieved. As such, the sampling radius cannot be too small otherwise the OAM measurement bandwidth will be limited,

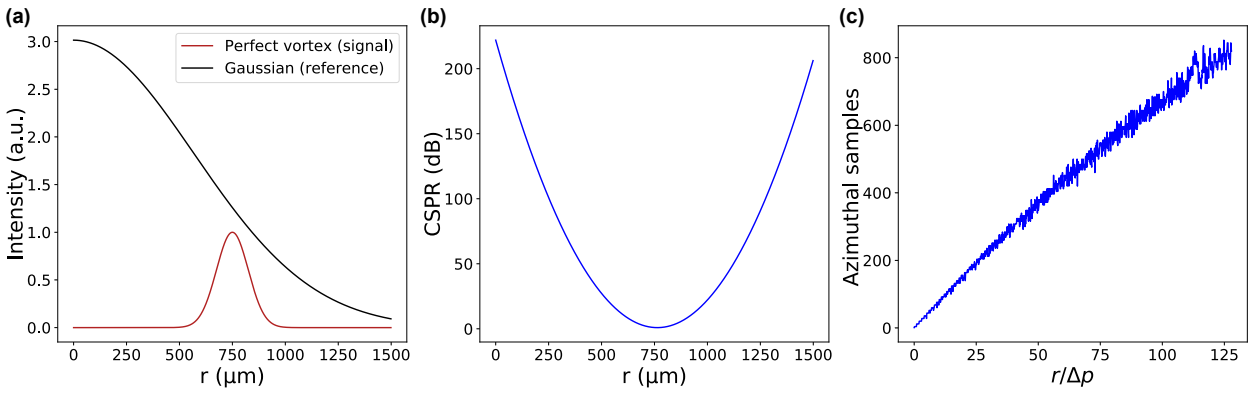


**Fig S9:** The effect of the sampling radius on the CSPR value and number of azimuthal samples. (a) Radial intensity distributions of the perfect vortex mode and reference Gaussian mode used in the experiment. At the radius of $750\ \mu\mathrm{m}$ we sample the interferogram, the intensity of the Gaussian mode is around 1 dB higher than the perfect vortex mode. (b) Radial CSPR values corresponding to the intensity distributions in (a). (c) The number of azimuthal samples at different radii. $\Delta p$ represents the pixel pitch size of the camera.

and this sets the limitation to perfectly retrieve fields with complex structures close to the beam center. Fortunately, OAM fields generally have hollow structures in the beam center. In our experimental setup, the resolution of the camera is $320 \times 256$ and the pixel pitch is $\Delta p = 30\ \mu\mathrm{m}$. The sampling radius of $750\ \mu\mathrm{m}$ gives 182 azimuthal samples.

## Supplementary Note 8. Simulation on the retrieval of Laguerre-Gaussian modes

In the main text, the KK method is used to retrieve perfect vortex beams at a fixed radius. The approach is readily to be generalized in two-dimensional space by decomposing the space into polar coordinates, and applying KK full-field retrieval to concentric rings. Similar to the one-dimensional case, the minimum phase condition needs to be satisfied for all theses rings. Although this poses constraints for inner circles close to the center due to the insufficient number of sampling, for OAM beams, their centers are generally dark resulted from the phase singularity and thus less an issue. In the following, we showcase the reconstruction of Laguerre-Gaussian (LG) modes, characterized by radial mode index $p$ and azimuthal mode index $l$, denoted as $\mathrm{LG}(p, l)$.

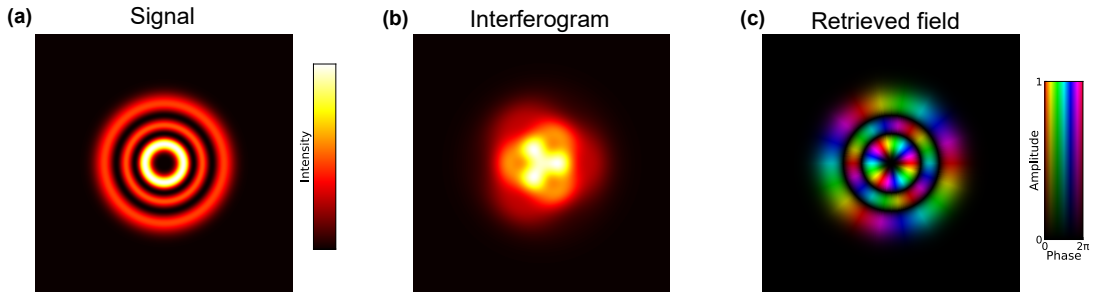


**Fig S10:** Simulated retrieval of LG modes. LG$(2, 3)$ mode is reconstructed as an example. (a) Intensity distribution, (b) intensity of the interferogram with a reference Gaussian beam, and (c) retrieved complex amplitude distribution of LG$(2, 3)$ mode.

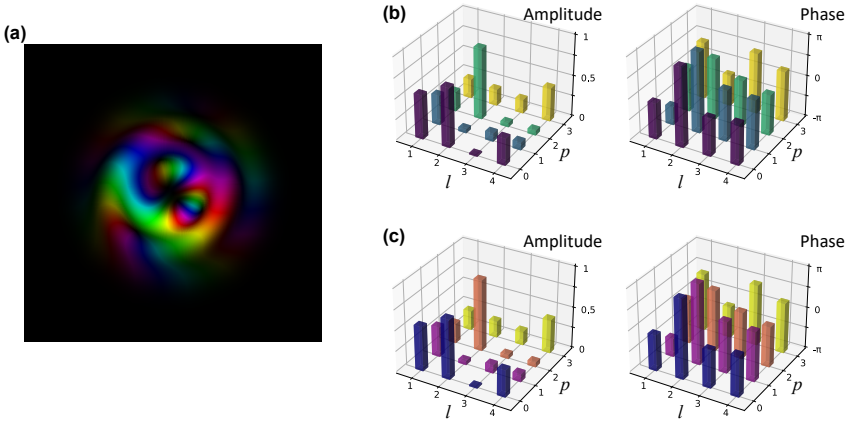


**Fig S11:** Simulated retrieval of the superposition of LG modes. The superposition of randomly weighted LG modes with $(p, l)$ indices in the range of $0 \leq p \leq 3, 1 \leq l \leq 4$ is reconstructed. (a) The complex amplitude distribution of the signal field. The LG mode decomposition (amplitude and phase) of (b) original and (c) retrieved fields.

Fig. S10 shows the simulation results on the retrieval of LG$(2, 3)$. The intensity distribution of the signal field and its interferogram with a reference Gaussian beam are shown in Fig. S10(a) and (b), respectively. By applying KK retrieval in the basis of concentric circles, the LG complex field can be reconstructed as shown in Fig. S10(c). As expected, the retrieved LG$(2, 3)$ mode shows $3$ nodal rings with alternating topological charge of $\pm 3$. In addition, we also show the retrieval of the superposition of LG modes. The signal field under test consists of randomly weighted LG modes with $(p, l)$ indices in the range of $0 \leq p \leq 3, 1 \leq l \leq 4$ , as shown in Fig. S11(a). Fig. S11(b) and (c) display respectively the LG mode decomposition of the original and retrieved superimposed LG fields, which are in excellent agreement with overlap integral reaching $99.98\%$. Here the slight discrepancy is attributed to the insufficient sampling close to the beam center as well as processing data in polar coordinate while being measured in Cartesian coordinate.